PHYSICAL SCIENCES

Ionic heat dissipation in solid-state pores

Makusu Tsutsui[1]*, Akihide Arima[2], Kazumichi Yokota[3], Yoshinobu Baba[2,4,5]*, Tomoji Kawai[1]*

Energy dissipation in solid-state nanopores is an important issue for their use as a sensor for detecting and analyzing individual objects in electrolyte solution by ionic current measurements. Here, we report on evaluations of heating via diffusive ion transport in the nanoscale conduits using thermocouple-embedded SiN_x pores. We found a linear rise in the nanopore temperature with the input electrical power suggestive of steady-state ionic heat dissipation in the confined nanospace. Meanwhile, the heating efficiency was elucidated to become higher in a smaller pore due to a rapid decrease in the through-water thermal conduction for cooling the fluidic channel. The scaling law suggested nonnegligible influence of the heating to raise the temperature of single-nanometer two-dimensional nanopores by a few kelvins under the standard cross-membrane voltage and ionic strength conditions. The present findings may be useful in advancing our understanding of ion and mass transport phenomena in nanopores.

INTRODUCTION

When electrical charges pass through a medium under a potential gradient, their kinetic energy is dispersed as heat upon inelastic interactions. This phenomenon is known as Joule heating, ubiquitous in any conductors larger than a characteristic mean free path. Electric field–driven ion transport through solid-state nanopores (*1*–*4*) is also predicted to involve heat dissipation as cations and anions move in crowds of water molecules. The fact that the ionic conductance is well described by a Maxwell model (*5*–*8*) clearly suggests the diffusive nature of the ion motions and concomitant Joule heat generation even in single-nanometer-scale nanopores. On the other hand, it remains almost unexplored how the ionic heating actually occurs because of the technical difficulty to probe local heat at the nanoscale conduits (*9*), despite the tremendous efforts devoted to single-particle and single-molecule analyses via resistive pulse measurements (*10*–*14*), along with the expected impact on translocation dynamics (*15*, *16*) as well as the ion transport properties (*17*, *18*). For example, high voltage applied to a solid-state nanopore was reported to induce characteristic ionic current fluctuations indicative of nanobubble nucleation (*19*, *20*). Furthermore, optical measurements using a fluorescent probe observed temperature increase in and outside a conical micropore in a polymeric membrane (*21*). Although these studies inferred substantial increase in the local temperature by energy dissipation (*19*–*21*), direct assessments of self-heating are yet to be performed. Here, we addressed this issue by embedding a nanothermometer in the vicinity of a nanopore to simultaneously record the temperature change upon voltage sweeps across the membrane.

RESULTS

The device consists of a 40-nm-thick SiN_x thin film suspended on a silicon wafer (Fig. 1, A to C; see also fig. S1 for details about the fabrication procedure). On the membrane, we formed a 100-nm-sized point contact made of Au and Pt nanowires that served as a thermometer. At the side of the thermal probe, a pore of diameter d_{pore} was sculpted. The whole structure was coated with a SiO_2 layer for preventing current leakage. The thermocouple was calibrated in individual experiments by measuring the change in the thermovoltage ΔV_{th} between the Au and Pt nanowires upon external heating by a resistive heater as described elsewhere (fig. S2) (*22*, *23*).

The ionic current through the thermometer-embedded pore I_{ion} was recorded together with ΔV_{th} under varying cross-membrane voltage V_b to probe local heat generated via energy dissipation (Fig. 1A). The I_{ion}-V_b characteristics of a 300-nm-sized nanopore demonstrated ohmic behavior in phosphate-buffered saline (PBS) containing 1.37 M NaCl (red curve in Fig. 2A, inset). At the same time, ΔV_{th} exhibited nonlinear rise under the positive and negative cross-membrane voltage (Fig. 2A). The corresponding temperature at the Au/Pt point contact T_t (fig. S2) suggested prominent heating of the nanopore by more than 30 K from the ambient at 1 V. Meanwhile, whereas the T_t response became weaker in diluter electrolyte solution of lower ionic strength (blue plots in Fig. 2A), we found that the results at different salt concentrations share the same linear relationship between T_t and the input power $P = I_{ion}V_b$ (Fig. 2B). This can be interpreted as signifying a steady-state change in the nanopore temperature under the balance between the local heating via the electric field–driven diffusive ion transport and the associated heat transport (*24*, *25*) [see also fig. S3 for the heating properties in a nanopore under a salt gradient, where we observed a highly asymmetric T_t-V_b behavior reflecting the electroosmotically driven diode-like I_{ion}-V_b characteristics (*26*)].

It is interesting to see how high the temperature can become by the local heating. For instance, theoretical estimations predicted superheating of electrolyte solution in a nanopore to above the boiling point (*19*, *27*). In the present study, on the other hand, whereas we observed linear T_t versus P characteristics in the repetitive V_b scans up to P = 18 μW in the nanopore of d_{pore} = 300 nm (green plots in Fig. 2C), further enlargement of the electrical load eventually led to irretraceable plots to immeasurable thermovoltage, wherein the pore temperature was raised to above 440 K (orange plots in Fig. 2C). In contrast, the I_{ion}-V_b curve remained stable even under the high-power condition, meaning no notable deformation of the robust SiN_x channel structure (*28*). The instability of the ΔV_{th} measurements at the high-V_b conditions thus indicated malfunction of

[1]The Institute of Scientific and Industrial Research, Osaka University, Mihogaoka 8-1, Ibaraki, Osaka 567-0047, Japan. [2]Institute of Nano-Life-Systems, Institutes of Innovation for Future Society, Nagoya University, Nagoya 464-8603, Japan. [3]National Institute of Advanced Industrial Science and Technology, Takamatsu, Kagawa 761-0395, Japan. [4]Department of Biomolecular Engineering, Graduate School of Engineering, Nagoya University, Furo-cho, Chikusa-ku, Nagoya 464-8603, Japan. [5]Institute of Quantum Life Science, National Institutes for Quantum and Radiological Science and Technology, Anagawa 4-9-1, Inage-ku, Chiba 263-8555, Japan.
*Corresponding author. Email: tsutsui@sanken.osaka-u.ac.jp (M.T.); babaymtt@chembio.nagoya-u.ac.jp (Y.B.); kawai@sanken.osaka-u.ac.jp (T.K.)

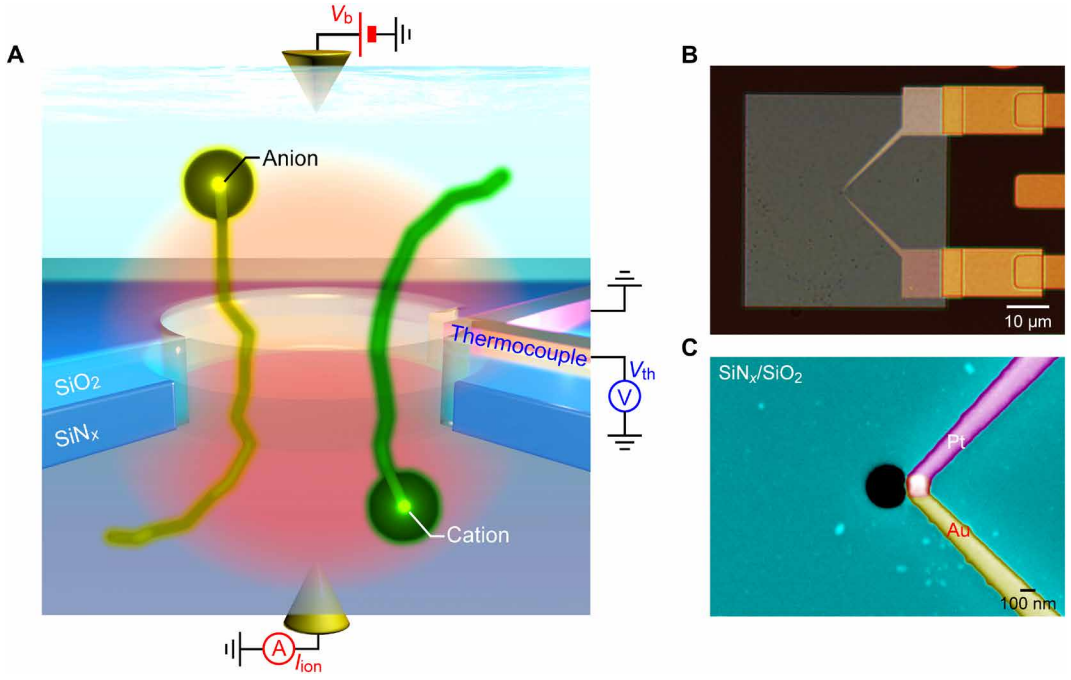

Fig. 1. Local heating in a solid-state nanopore. (**A**) A schematic model depicting simultaneous measurements of ionic current I_{ion} and local temperature at a nanopore. Diffusive ion transport in salt solution under the applied cross-membrane voltage V_b induces energy dissipation to local heating at the nanopore, whose effect was evaluated by recording the thermovoltage change V_{th} at the thermocouple embedded in the vicinity of the channel. (**B** and **C**) Optical image (B) and false-colored scanning electron micrograph (C) of a 300-nm-sized thermometer-embedded nanopore. Square region in (B) is the SiO_2/SiN_x membrane. The thermometer consisted of a 100-nm-sized point contact made of Pt and Au nanowires lithographed at the side of the nanopore (C).

the metallic nanothermometer by the ionic heating. Checking the endurance of the thermocouple, we observed severe damage on the Au nanowire when advertently heating it to 573 K while leaving the Pt component intact (fig. S4). The phenomenon detected at the high-P regime is hence attributed to the thermally induced breakdown of the nanoscale Au line (*29*) by the dissipated heat in the nanopore. The results unambiguously prove the significant role of energy dissipation capable to heat up the nanopore to above the boiling point of water (see also figs. S5 to S7 for the ionic current characteristics under $V_b > 3$ V) (*19*, *27*).

The pronounced local heating anticipates marked change in the ion transport characteristics (*16*, *17*). In this regard, the open pore conductance G was found to increase steadily with increasing V_b (Fig. 3A), ascribable to the influence of the energy dissipation. Specifically, G is given by the Maxwell model (*5*–*8*) as $G = (R_{pore} + R_{acc})^{-1}$, where $R_{pore} = 4\rho L_{pore}/\pi {d_{pore}}^2$ and $R_{acc} = \rho/d_{pore}$ are the resistance inside and outside the pore, respectively. Assuming the depth L_{pore} and the diameter d_{pore} of the nanopore remain unaltered during the voltage scans, which is very likely to be the case since no hysteresis was found in the I_{ion} versus V_b curves, contributions of the electrical heating were expected to enter through the conductivity $\sigma = \rho^{-1} = n_c e\mu_c + n_a e\mu_a$, where $n_{c,a}$ and $\mu_{c,a}$ are, respectively, the number and the mobility of cations and anions. Here, $\mu_{c,a}$ is further given as $\mu_{c,a} = Q/4\pi\eta r_{c,a}$ in the framework of Stokes law (*30*), predicting viscous drag force $F_{drag} = 4\pi\eta r_{c,a} v_{c,a}$ acting on the cations and anions moving at the drift velocity $v_{c,a}$ in a liquid of viscosity η. Consequently, we arrive at a simple expression $G \sim \beta/\eta$, where β is the coefficient defined by the nanopore structure as well as the ion radii and concentrations tentatively taken as constants. Using semiempirical formula (*31*), we deduced η as a function of T_t where we approximated the viscosity of the electrolyte buffer to be the same as that of water. It predicted less viscous fluid in the self-heated pore at the elevated V_b (Fig. 3B). The result demonstrated linear dependence of G on η^{-1} (Fig. 3C), consistent to the classical Walden rule (*32*). While this manifests the notable effects of ionic heating on the open pore conductance, its actual influence is not so significant, increasing the conductance by only about 10% under 100 K rise in T_t, which is presumably due to the fact that whereas the conductance is dominated by the conductivity outside the pore as $R_{acc} >> R_{pore}$ for $d_{pore} = 300$ nm and $L_{pore} = 50$ nm (*6*), the temperature rise takes place mainly in the nanopore, thus leaving a large portion of the access resistance unchanged.

To investigate whether this is a common feature in fluidic channels of different sizes, we extended the measurements to thermometer-embedded pores of various diameters ranging from 10 μm to 100 nm (see figs. S8 to S12). All of these conduits displayed linear η^{-1} versus G characteristics. Meanwhile, the slopes β were found to scale linearly with d_{pore} (Fig. 3D). This signifies equal effectiveness of the local heating on the ionic conductance irrespective of the channel size, considering the fact that $G \sim {R_{acc}}^{-1} \sim d_{pore}$, and hence, $\beta \sim d_{pore}$, for the low depth-to-diameter aspect ratio pores (*5*–*7*).

The local heat dissipation is also expected to yield large noise considering its outcome to induce thermal agitation of ions at the nanopores (*33*). Fast Fourier transform analyses of I_{ion} traces provided noise spectra at various V_b (Fig. 4A; see also fig. S13). Under low cross-membrane voltage, the power spectrum density I_{noise} showed

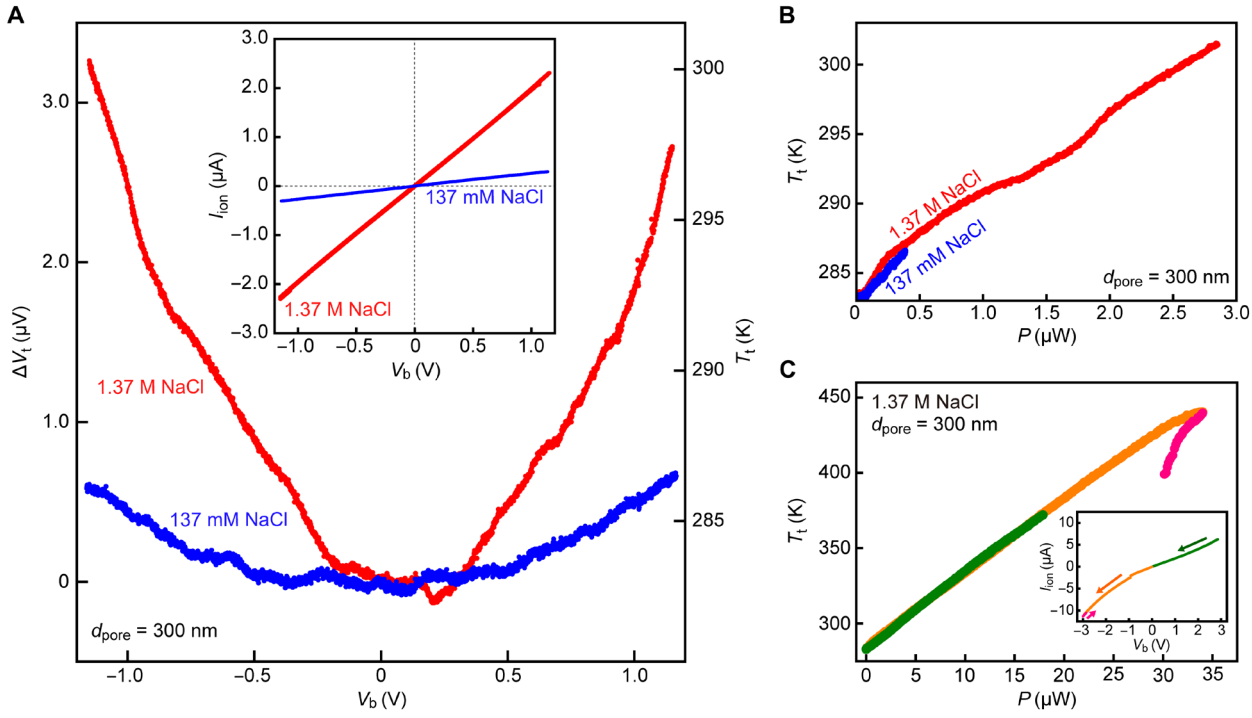

Fig. 2. Simultaneous measurements of ionic current and local temperature at a nanopore. (**A**) Changes in the thermovoltage ΔV_{th} and the corresponding local temperature T_{th} at the thermocouple against the voltage V_b applied across the 40-nm-thick SiO_2/SiN_x membrane holding a nanopore of 300 nm diameter. Red and blue plots are the results obtained in phosphate-buffered saline (PBS) of ion concentration 1.37 M and 137 mM, respectively. Inset is the simultaneously recorded ionic current I_{ion} versus V_b curves. (**B**) Plots of T_t of (A) as a function of the electric power $P = I_{ion}V_b$. Color code is the same as that in (A). (**C**) Temperature response against larger input power in a 300-nm-sized nanopore. The curve became irretraceable when excessive power was loaded over 30 μW. In contrast, the I_{ion}-V_b characteristics was observed to be stable as shown in the inset, indicating failure of the thermocouple under the dissipated heat at the nanopore.

a characteristic profile typical for solid-state nanopores composed of surface charge fluctuation–derived 1/*f* feature at the low-frequency regime below 1 kHz and capacitance-mediated noise at above 10 kHz (*34*). Meanwhile, increase in V_b led to monotonic up-shift of the spectra (fig. S13). The trend can be seen more clearly in the plots of the noise intensity I_{th} at 2 kHz, demonstrating linear rise with the input electrical power (Fig. 4B), which suggests steady increase in the thermal noise in response to the increase in the nanopore temperature via the local heating. At higher temperatures, on the other hand, the noise intensity levels off due presumably to the fact that the thermal noise became more pronounced than the capacitance-derived high-frequency component (*34*).

Last, we inspect the mechanism underlying the energy dissipation by comparing the heating properties in pores of different diameter. Measuring the local temperature at the point contact of the nanothermocouple under the applied ramp cross-membrane voltage, T_t tended to increase linearly with P regardless of the size of the fluidic channels ranging from d_{pore} = 10 μm to 100 nm (Fig. 5A). Meanwhile, as evident in the figure, it costed higher electrical power to heat up larger pores. To shed light on the scaling law, the efficiency of the ionic heating was evaluated by deducing $C = P/T_t$ from the linear dependence of the nanopore temperature on the load power. Plotting as a function of the pore diameter, C was found to scale linearly with d_{pore} (Fig. 5B). The trend can be qualitatively explained in a framework of Fourier's law that renders the interplay of the local power dissipation P at the nanopore and concomitant heat flow via the effective thermal conductance K at the both sides of the channel as $P = 2K(T_t - T_0)$, where T_0 is the surrounding temperature. Assuming hemispheres of water with diameter d_w were involved in the heat spread, $K \sim d_w$ and hence $P/T_t = C \sim d_w$. Figure 5A can thus be interpreted as reflecting $d_w \sim d_{pore}$, suggestive of energy dissipation at more expansive area at the orifices of larger pores that consumes more power to heat up the channel.

The above physical picture presumes that the thermal conduction through water plays a predominant role on the heat spread at the nanopores. Meanwhile, the electroosmosmotic flow in the voltage-biased nanopores anticipates heat transfer via convection. We therefore evaluated these two heat transport mechanisms by numerically solving a continuum heat transfer problem with a finite element method (figs. S14 to S16). The effectiveness of the convection to carry the ionic heat away from the nanopores was found to be little compared to the heat conduction counterpart.

The electrical heating mechanism was further verified by examining the nanopore measurements in liquid of different thermodynamic properties. As a model case, we used glycerol having specific heat capacity of c_{gly} = 2390 J/kgK, which is about a factor of 2 smaller than that of water c_w = 4182 J/kgK. The local temperature at a 3-μm-sized pore in 1: 1 mixture of glycerol and PBS showed linear increase with P, analogous to that in the electrolyte buffer (fig. S17). In contrast, the rate of T_t increase was found to be more rapid due to the lower heat capacity involved in the local heating. More quantitatively, the specific heat capacity of the glycerol/PBS c_{mix} is

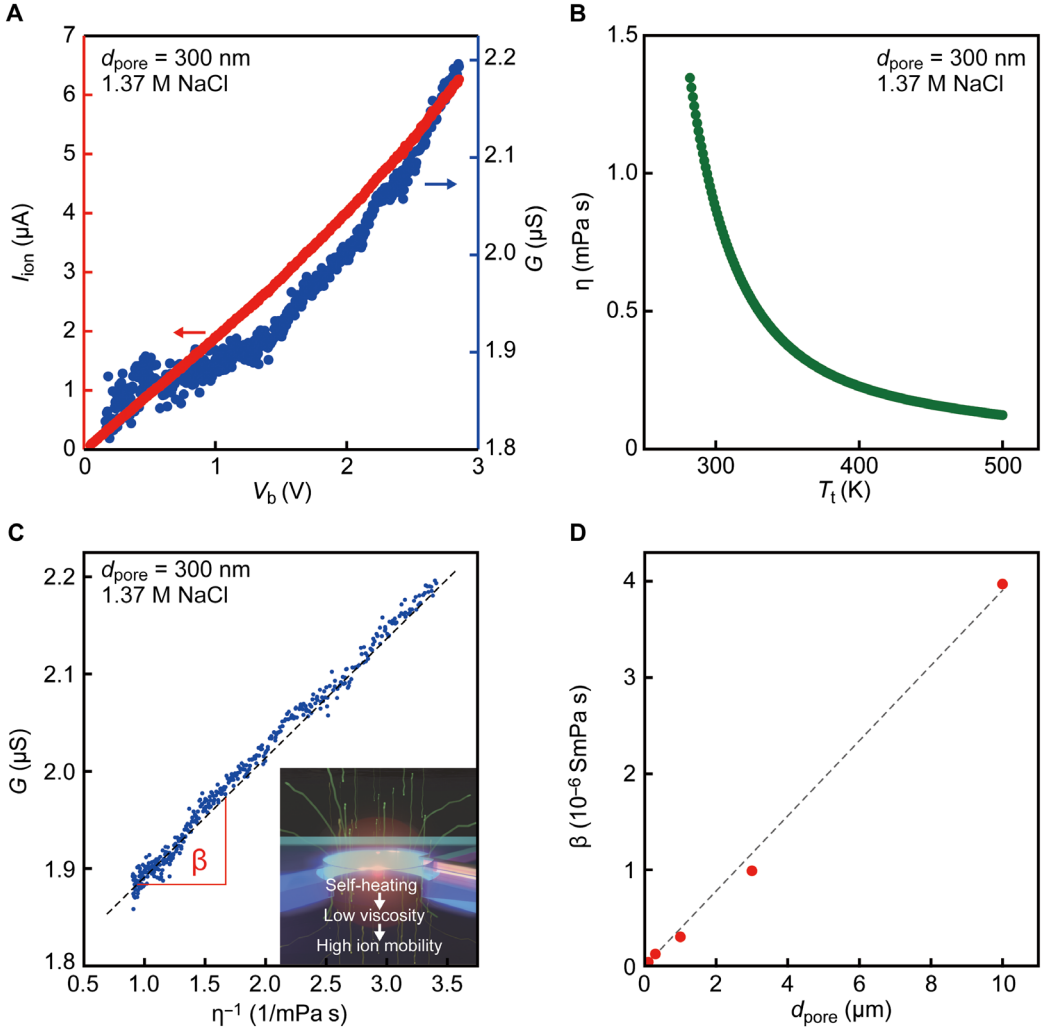

Fig. 3. Ion transport in self-heated nanopores. (**A**) The ionic current I_{ion} (red) and the conductance G (blue) in a 300-nm-sized nanopore filled with electrolyte buffer containing 1.37 M NaCl under a voltage scan from 0 to 3 V. (**B**) Theoretically predicted water viscosity change η associated with the temperature increase at the nanopore. (**C**) Linear dependence of G on η^{-1} revealing pronounced effects of heat dissipation–mediated viscosity change on the ionic current characteristics. Red line is a linear fit defining a slope β. (**D**) Linear relation between β and the pore diameter d_{pore} from 100 nm to 10 μm. Dashed line is a linear fitting to the plots.

given as $c_{mix} = (m_w c_w + m_{gly} c_{gly})/(m_w + m_{gly})$, where m_w and m_{gly} are the mass of the water and the glycerol, respectively (assuming the density and specific capacity of the electrolyte buffer as those of water). With the density of 1.25 g/ml of glycerol, c_{mix} is deduced as 3186 J/kgK. On the other hand, the heating efficiency C is deduced from the T_t-P plots (fig. S17C) as C_{mix} = 849 nW/K and C_{PBS} = 1145 nW/K. Comparing the results, we found that the ratio between C_{mix} and C_{PBS} (C_{PBS}/C_{mix} = 1.35) is in fair agreement with the relative difference in the specific heat capacities (c_w/c_{mix} = 1.31). This manifests the important role of the liquid heat capacity at the pore orifice where the electrokinetic energy of ions is mostly dissipated, which, in turn, indicates a minor influence of solid-state compartments such as the SiN_x wall and the metallic thermometer due, in part, to the relatively small specific heat capacities on the order of 100 J/kgK. More specifically, the finite element analyses of the ionic heat dissipation elucidated rather uniform temperature distributions, with only 21% underestimation of the 300-nm nanopore temperature by T_t (fig. S18A). Meanwhile, we add to note that this error becomes slightly larger for smaller pores, 24% for the 100-nm-sized nanopore (fig. S18B), ascribed to the more pronounced influence of heat loss at the SiN_x for their deteriorated cooling capability via heat conduction through water. This may be a reason why the plots deviate more at the low d_{pore} regime in Fig. 5B.

Extrapolating the d_{pore} dependence (Fig. 5C), we estimated the impact of the local heating in smaller nanopores of diameter 10 and 1 nm with low–aspect ratio structure, the designs of which have been widely used for sensing proteins (*35*–*37*) and genomes (*38*). In 1 M KCl, for instance, it predicts a notable increase in the pore temperature by 10 K above the ambient for a 10-nm-sized nanopore of 10 nm depth under V_b = 1.0 V, where we obtained the open pore conductance from the Maxwell model (*8*) with a bulk conductivity of the KCl solution (*39*). The result is similar in the case of a 1-nm-diameter pore in a two-dimensional material of 0.6 nm effective thickness (*5*). Increasing the salt concentration to 4 M KCl, on the other hand, the local heating becomes more pronounced, raising the temperature at the nanochannel by more than 57 K at 1 V. It

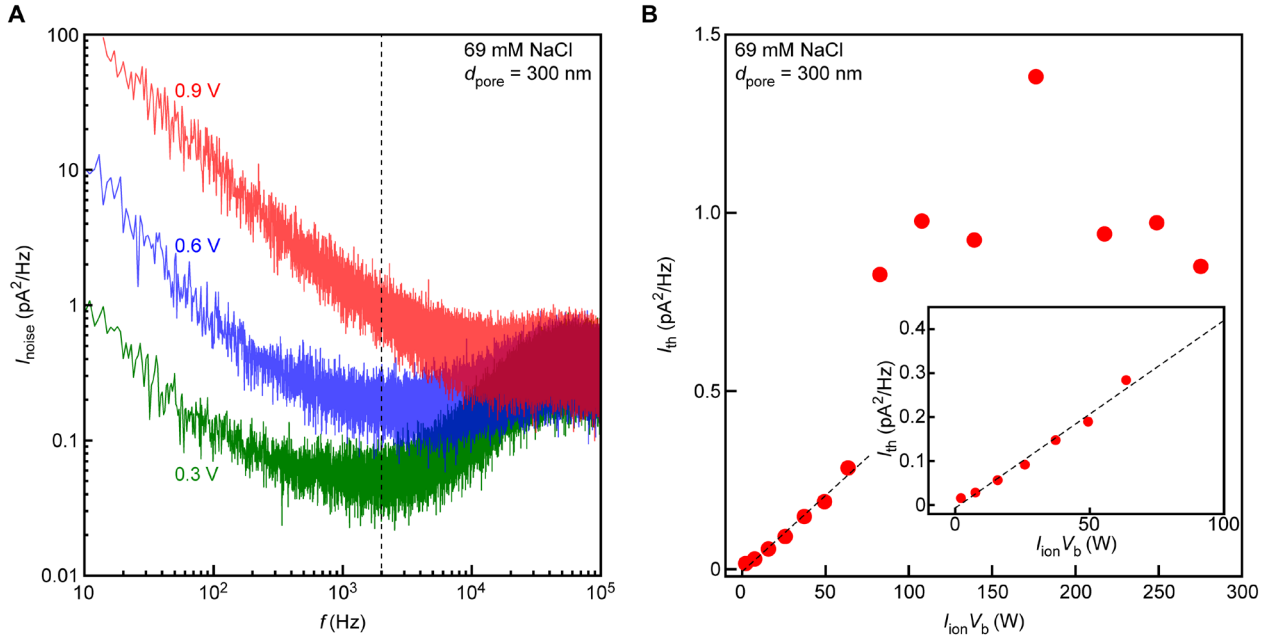

Fig. 4. Cross-membrane voltage–dependent noise spectra. (**A**) Overplots of noise spectra obtained at $V_b = 0.3$ V (green), 0.6 V (blue), and 0.9 V (red), which showed a monotonic upward shift with increasing V_b. Dashed line indicates $f = 2$ kHz. (**B**) Plots of the noise intensity I_{th} at $f = 2$ kHz as a function of the input electrical power. Inset shows a magnified view at a low-power regime. Dashed lines are linear fits at $I_{ion}V_b < 100$ W.

would thus be of crucial importance to take the Joule heating into account in the nanopore sensing as these conditions are normally used for single-molecule analyses by ionic current.

DISCUSSION

We elucidated the pronounced effects of energy dissipation in solid-state nanopores causing significant local heating under typical experimental conditions. While it was demonstrated to affect the ionic conductance via the induced change in the viscosity, the electrically formed heat spot is also anticipated to alter the capture-to-translocation dynamics of analytes. For example, it foresees structural change of soft biomolecules such as proteins and amyloids (*40*, *41*) that should be considered in an attempt to resolve the conformational changes by the blockade current (*13*, *35*). Meanwhile, it would facilitate DNA to denature into single-stranded forms, an important aspect for implementing single-molecule sequencing with solid-state nanopores (*3*, *42*). Moreover, the induced temperature gradient at the orifices may bring thermophoretic forces to draw analytes into pores that contributes to better throughput of resistive pulse sensing (*15*, *16*). Future efforts should be devoted to verify the roles of self-heating on these unique capabilities of solid-state nanopores.

MATERIALS AND METHODS

Fabrication of thermometer-embedded nanopores

A 40-nm-thick SiN_x-coated, 4-inch silicon wafer was diced into 30 mm–by–30 mm pieces with a dicer. On the SiN_x surface, microelectrodes were formed by photolithography followed by radio-frequency magnetron sputtering (Samco) of a 20-nm-thick Ti/Au layer and subsequent liftoff by ultrasonication in *N*,*N*-dimethylformamide (DMF; Wako). A nanowire was then delineated by electron beam lithography (Elionix) using ZEP520A (Zeon). In the pattern, there was also a nanoscale cross drawn at a predefined position. After development, the entire surface was coated with a 20-nm-thick Pt layer by sputtering and was lifted off in DMF. The series of the electron beam lithography and metal deposition processes were then implemented to form a 20-nm-thick Au nanowire so as to create the nanothermocouple consisting of a 100-nm-sized Au/Pt point contact, wherein the nanoscale cross was used as a marker to align the tips of the two nanowires. After that, the Si beneath the thermometer was wet-etched in heated KOH aq. (Sigma-Aldrich) through a 1-mm-sized window made in the SiN_x layer on the back side of the substrate by reactive ion etching with a metal mask. As a result, we obtained a SiN_x membrane supporting the thermometer. A pore of various diameters ranging from 10 μm to 100 nm was then sculpted at the vicinity of the thermometer by electron beam lithography and reactive ion etching, again using the nanocross as a marker. Last, the entire surface was covered with a 40-nm-thick SiO_2 from the top by chemical vapor deposition.

Thermometer calibration

The Pt/Au thermometer was calibrated by a procedure described elsewhere (*22*, *23*). Briefly, the thermometer sample was sealed in a vacuum chamber and evacuated to a level below 10^{-5} torr. The point contact was then heated via electrical heating of a resistive heater to a set temperature. Confirming that the temperature became stable, the thermovoltage at the Pt/Au thermometer was recorded using a Keithley 2182A nanovoltmeter. The series of the processes were performed in a temperature range from 300 to 600 K. The temperature dependence of the thermovoltage was used to calculate the thermometer temperature rise during the cross-membrane voltage scans.

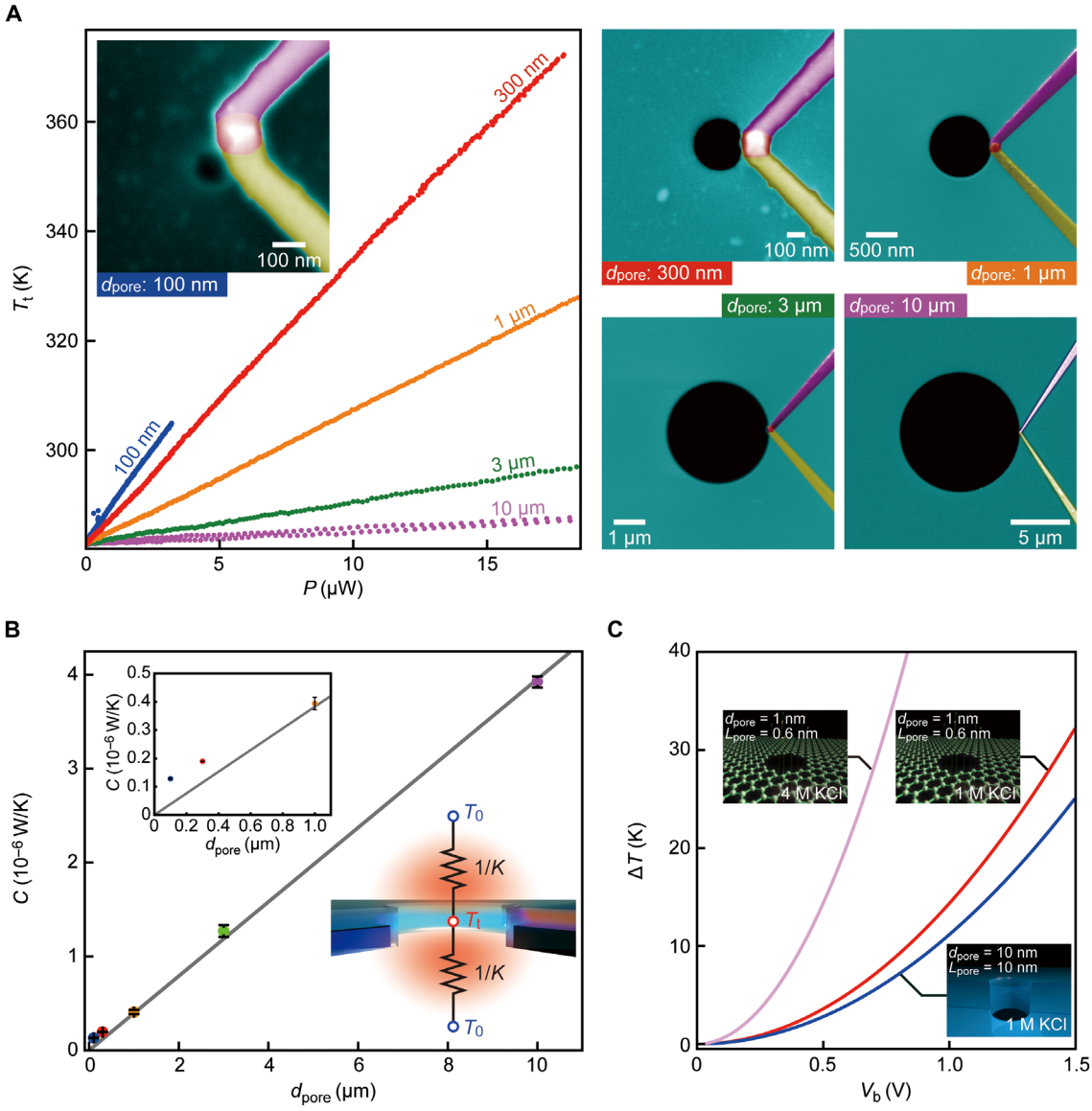

Fig. 5. Local heating in solid-state pores. (**A**) T_t-P characteristics in pores of various sizes from 100 nm to 10 μm. Images are the false-colored scanning electron micrographs displaying the structure of the thermometer-embedded pores used. The local temperature tends to be raised under lower electric power for smaller channels, attributed mainly to the lower water heat capacity involved in the heating. (**B**) Plots of the power cost C to raise the local temperature by 1 K with respect to d_{pore}. The gray curve is a linear fit with zero intercept indicating C increase with d_{pore}. Insets are an equivalent circuit depicting steady-state heat flow under the temperature difference of T_t and the bath temperature T_0 via the thermal resistance $1/K$ and a magnified view at small d_{pore}. (**C**) Predicted change in the temperature ΔT at nanopores of diameter d_{pore} = 10 nm in a 10-nm-thick membrane (blue) and a 1-nm-sized channel mimicking a graphene nanopore structure (red) under the applied voltage V_b in 1 M KCl. A case of 4 M KCl is also shown for the 1-nm nanopore (pink).

Nanopore sealing

Polyimide blocks having microchannels at one side of the surface were prepared by curing polydimethylsiloxane (PDMS; Sylgard184, Dow) precursor on a photo-patterned SU-8 mold on a Si wafer, followed by baking for polymerization and cutoff with a knife. In each PDMS block, we punched three through-holes. The PDMS and the thermometer-embedded nanopore chip were then treated with oxygen plasma for surface activation. After that, they were put together for eternal bonding of the PDMS on the nanopore substrate. The process was repeated again to adhere another PDMS block to the other side of the Si chip.

Ionic current and nanopore temperature measurements

PBS (Wako) was poured into the nanopore through the inlet and outlet holes punched in the PDMS. The ionic current I_{ion} between a pair of Ag/AgCl rods placed in the remaining holes in the polymer blocks was then measured under the applied cross-membrane voltage V_b using a Keithley 6487 (Keithley) picoammeter. At the same time, the thermovoltage V_{th} of the Au/Pt thermometer was recorded through the microelectrodes using a Keithley 2182A nanovoltmeter. The measurement setup was General Purpose Interface Bus (GPIB)-controlled under a program coded in Visual Basic to record V_{th} upon V_b change by 1 mV.

Finite element simulations

The temperature distribution in a nanopore under applied cross-membrane voltage was described by a heat equation based on Joule heating source terms of $J{\cdot}E$, where J and E are the current density and the applied electric field, respectively (*19*). The steady-state heat equations for (Eq. 1) solids and (Eq. 2) fluids are respectively expressed as

$$\nabla{\cdot}(\kappa\,\nabla\,T)+J\cdot E\;=\;0 \tag{1}$$

and

$$\nabla{\cdot}(\kappa\,\nabla\,T)+J\cdot E=\rho_{\mathrm{d}}\,C_{\mathrm{p}}\,u\cdot\nabla T \tag{2}$$

Here, κ, T, ρ_{d}, C_{p}, and u are the thermal conductivity, temperature, density, heat capacity, and fluid velocity field, respectively. The current density in these equations was coupled to the continuity equation at a steady state

$$\nabla{\cdot}J\;=\;0 \tag{3}$$

From Ohm's law, J is proportional to E as $J=\sigma E$, where σ is the conductivity. The temperature dependence of the bulk electrical conductivity for the electrolyte solution was evaluated from the relation of $G(T)=(4\rho L_{\mathrm{pore}}/\pi {d_{\mathrm{pore}}}^2+\rho/d_{\mathrm{pore}})^{-1}$. The mobilities of anions (μ_{a}) and cations (μ_{c}) were obtained as $\mu_{\mathrm{a,c}}=\sigma/(20eN_{\mathrm{A}}c_0)$ where $N_{\mathrm{A}}=6.02\times10^{23}\ \mathrm{mol}^{-1}$ is the Avogadro constant. The number density distribution of anions (n_{a}) and cations (n_{c}) for the nanopore was calculated by using the Nernst-Planck equation

$$\nabla{\cdot}\left(-\frac{u_{\mathrm{a,c}}k_{\mathrm{B}}T}{e}\nabla n_{\mathrm{a,c}}-z_{\mathrm{a,c}}\,n_{\mathrm{a,c}}\,eu_{\mathrm{a,c}}\nabla\phi\right)+u\cdot\nabla n_{\mathrm{a,c}}=0 \tag{4}$$

Here, k_{B}, e, $z_{\mathrm{a,c}}$, and φ are the Boltzmann constant ($k_{\mathrm{B}}=1.38\times10^{-23}$ J/K), elementary charge ($e=1.60\times10^{-19}$ C), charge number of ions ($z_{\mathrm{c}}=1$ for Na^+ and $z_{\mathrm{a}}=-1$ for Cl^-), and electrostatic potential. The distribution of φ was solved by using the Poisson-Boltzmann equation

$$\nabla^2\phi\;=\;-\frac{\rho_Q}{\varepsilon_{\mathrm{w}}}\;=\;-\frac{e}{\varepsilon_{\mathrm{w}}}\sum_{\mathrm{a,c}}z_{\mathrm{a,c}}\,n_{\mathrm{a,c}}\exp\left(-\frac{z_{\mathrm{a,c}}\,e\phi}{k_{\mathrm{B}}\,T}\right) \tag{5}$$

Here, ρ_Q and ε_{w} are the electric charge density and permittivity of water. The temperature dependence of $\varepsilon_{\mathrm{w}}=(249-0.790\mathrm{T}+7.30\times10^{-4}\,T^2)\varepsilon_0$ was assumed where ε_0 is the electric constant of 8.85×10^{-12} F/m. Through the coupling between ρ_Q and E, the force $\rho_Q E$ generates the electroosmotic flow. The resulting heat convection was simulated by using the incompressible Navier-Stokes equation for hydrodynamic pressure p and fluid velocity field u

$$-\nabla p+\eta\nabla^2u+\rho_Q E\;=\;0 \tag{6}$$

Eqs. 1 to 6 were simultaneously solved by using a software package for finite element methods of COMSOL Multiphysics 5.5 (COMSOL Inc., Stockholm, Sweden).

SUPPLEMENTARY MATERIALS

Supplementary material for this article is available at https://science.org/doi/10.1126/sciadv.abl7002

REFERENCES AND NOTES

1. J. Li, C. McMullan, D. Branton, M. J. Aziz, J. A. Golovchenko, Ion-beam sculpting at nanometre length scales. *Nature* **412**, 166–169 (2001).
2. C. Dekker, Solid-state nanopores. *Nat. Nanotechnol.* **2**, 209–215 (2007).
3. D. Branton, D. W. Deamer, A. Marziali, H. Bayley, S. A. Benner, T. Bulter, M. Di Ventra, S. Garaj, A. Hibbs, X. Huang, S. B. Jovanovich, P. S. Krstic, S. Lindsay, X. S. Ling, C. H. Mastrangelo, A. Meller, J. S. Oliver, Y. V. Pershin, J. M. Ramsey, R. Riehn, G. V. Soni, V. Tabard-Cossa, M. Wanunu, M. Wiggin, J. A. Schloss, The potential and challenges of nanopore sequencing. *Nat. Biotechnol.* **26**, 1146–1153 (2008).
4. M. Drndic, Sequencing with graphene pores. *Nat. Nanotechnol.* **9**, 743 (2014).
5. S. Garaj, W. Hubbard, A. Reina, J. Kong, D. Branton, J. A. Golovchenko, Graphene as a subnanometre trans-electrode membrane. *Nature* **467**, 190–193 (2010).
6. S. W. Kowalczyk, A. Y. Grosberg, Y. Rabin, C. Dekker, Modeling the conductance and DNA blockade of solid-state nanopores. *Nanotechnology* **22**, 315101 (2011).
7. M. Tsutsui, S. Hongo, Y. He, M. Taniguchi, N. Gemma, T. Kawai, Single-nanoparticle detection using a low-aspect-ratio pore. *ACS Nano* **6**, 3499–3505 (2012).
8. S. Sahu, M. Zwolak, Colloquium: Ionic phenomena in nanoscale pores through 2D materials. *Rev. Mod. Phys.* **91**, 021004 (2019).
9. J.-M. Yang, Z.-Q. Pan, F.-F. Qin, M. Chen, K. Wang, X.-H. Xia, An in situ SERS study of ionic transport and the Joule heating effect in plasmonic nanopores. *Chem. Commun.* **54**, 13236–13239 (2018).
10. T. Albrecht, Single-molecule analysis with solid-state nanopores. *Annu. Rev. Anal. Chem.* **12**, 371–387 (2019).
11. L. Xue, H. Yamazaki, R. Ren, M. Wanunu, A. O. Ivanov, J. B. Edel, Solid-state nanopore sensors. *Nat. Rev. Mater.* **5**, 931–951 (2020).
12. Y. He, M. Tsutsui, Y. Zhou, X.-S. Miao, Solid-state nanopore systems: From materials to applications. *NPG Asia Mater.* **13**, 48 (2021).
13. N. Varongchayakul, J. Song, A. Meller, M. W. Grinstaff, Single-molecule protein sensing in a nanopore: A tutorial. *Chem. Soc. Rev.* **47**, 8512–8524 (2018).
14. K. Lee, K.-B. Park, H.-J. Kim, J.-S. Yu, H. Chae, H.-M. Kim, K.-B. Kim, Recent progress in solid-state nanopores. *Adv. Mater.* **30**, 1704680 (2018).
15. M. Zhang, C. Ngampeerapong, D. Redin, A. Ahmadian, I. Sychugov, J. Linnros, Thermophoresis-controlled size-dependent DNA translocation through an array of nanopores. *ACS Nano* **12**, 4574–4582 (2018).
16. M. Belkin, C. Maffeo, D. B. Wells, A. Aksimentiev, Stretching and controlled motion of single-stranded DNA in locally heated solid-state nanopores. *ACS Nano* **7**, 6816–6824 (2013).
17. L. Payet, M. Martinho, C. Merstorf, M. Pastoriza-Gallego, J. Pelta, V. Viasnoff, L. Auvray, M. Muthukumar, J. Mathe, Temperature effect on ionic current and ssDNA transport through nanopores. *Biophys. J.* **109**, 1600–1607 (2015).
18. D. V. Verschueren, M. P. Jonsson, C. Dekker, Temperature dependence of DNA translocations through solid-state nanopores. *Nanotechnology* **26**, 234004 (2015).
19. E. V. Levine, M. N. Burns, J. A. Golovchenko, Nanoscale dynamics of Joule heating and bubble nucleation in a solid-state nanopore. *Phys. Rev. E* **93**, 013124 (2016).
20. S. Paul, W.-L. Hsu, M. Magnini, L. R. Mason, Y.-L. Ho, O. K. Matar, H. Daiguji, Single-bubble dynamics in nanopores: Transition between homogeneous and heterogeneous nucleation. *Phys. Rev. Res.* **2**, 043400 (2020).
21. V. Viasnoff, U. Bockelmann, A. Meller, H. Isambert, L. Laufer, Y. Tsori, Localized Joule heating produced by ion current focusing through micron-size holes. *Appl. Phys. Lett.* **96**, 163701 (2010).
22. L. Shi, A. Majumdar, Recent developments in micro and nanoscale thermometry. *Microscale Thermophys. Eng.* **5**, 251–265 (2001).
23. M. Tsutsui, T. Morikawa, K. Yokota, M. Taniguchi, Remote heat dissipation in atom-sized contacts. *Sci. Rep.* **8**, 7842 (2018).
24. J. R. Welty, C. E. Wicks, R. E. Wilson, G. Rorrer, *Fundamentals of Momentum, Heat, and Mass Transfer* (Wiley, 2001).
25. R. Menzel, S. Barg, M. Miranda, D. B. Anthony, S. M. Bawaked, M. Mokhtar, S. A. Al-Thabaiti, S. N. Basahel, E. Saiz, M. S. P. Shaffer, Joule heating characteristics of emulsion-templated graphene aerogels. *Adv. Funct. Mater.* **25**, 28–35 (2015).
26. I. W. Leong, M. Tsutsui, S. Murayama, Y. He, M. Taniguchi, Electroosmosis-driven nanofluidic diodes. *J. Phys. Chem. B* **124**, 7086–7092 (2020).
27. G. Nagashima, E. V. Levine, D. P. Hoogreheide, M. M. Burns, J. A. Golovchenko, Superheating and homogeneous single bubble nucleation in a solid-state nanopore. *Phys. Rev. Lett.* **113**, 024506 (2014).
28. C. Leung, K. Briggs, M.-P. Laberge, S. Peng, M. Waugh, V. Tabard-Cossa, Mechanisms of solid-state nanopore enlargement under electrical stress. *Nanotechnology* **31**, 44LT01 (2020).
29. G. Ouyang, G. Yang, G. Zhou, A comprehensive understanding of melting temperature of nanowire, nanotube and bulk counterpart. *Nanoscale* **4**, 2748–2753 (2012).
30. M. Salanne, C. Simon, P. Turq, P. A. Madden, Conductivity-viscosity-structure: Unpicking the relationship in an ionic liquid. *J. Phys. Chem.* **111**, 4678–4684 (2007).
31. J. Kestin, M. Sololov, W. A. Wakeham, Viscosity of liquid water in the range −8 °C to 150 °C. *J. Phys. Chem. Ref. Data Monogr.* **7**, 941–948 (1978).

32. E. Szwajczak, A. Szymanski, On the relation between mobility of Ions and viscosity. The Walden's Rule. *Mol. Cryst. Liq. Cryst.* **139**, 253–261 (1986).
33. C. Wen, S. Zeng, K. Arstila, T. Sajavaara, Y. Zhu, Z. Zhang, S.-L. Zhang, Generalized noise study of solid-state nanopores at low frequencies. *ACS Sens.* **2**, 300–307 (2017).
34. J. K. Rosenstein, M. Wanunu, C. A. Merchant, M. Drndic, K. L. Shepard, Integrated nanopore sensing platform with sub-microsecond temporal resolution. *Nat. Methods* **9**, 487–492 (2012).
35. P. Waduge, R. Hu, P. Bandarkar, H. Yamazaki, B. Cressiot, Q. Zhao, P. C. Whitford, M. Wanunu, Nanopore-based measurements of protein size, fluctuations, and conformational changes. *ACS Nano* **11**, 5706–5716 (2017).
36. W. Si, A. Aksimentiev, Nanopore sensing of protein folding. *ACS Nano* **11**, 7091–7100 (2017).
37. E. Kennedy, Z. Dong, C. Tennant, G. Timp, Reading the primary structure of a protein with 0.07 nm^3 resolution using a subnanometre-diameter pore. *Nat. Nanotechnol.* **11**, 968–976 (2016).
38. J. A. Rodriguez-Manzo, M. Puster, A. Nicolai, V. Manuier, M. Drndic, DNA translocation in nanometer thick silicon nanopores. *ACS Nano* **9**, 6555–6564 (2015).
39. M. L. Kovarik, K. Zhou, S. C. Jacobson, Effect of conical nanopore diameter on ion current rectification. *J. Phys. Chem. B* **113**, 15960–15966 (2009).
40. M. Noji, T. Samejima, K. Yamaguchi, M. So, K. Yuzu, E. Chatani, Y. Akazawa-Ogawa, Y. Gagihara, Y. Kawata, K. Ikenaka, H. Mochizuki, J. Kardos, D. E. Otzen, V. Bellotti, J. Buchner, Y. Goto, Breakdown of supersaturation barrier links protein folding to amyloid formation. *Commun. Bio.* **4**, 120 (2021).
41. Y. Kusumoto, A. Lomakin, D. B. Teplow, G. B. Benedek, Temperature dependence of amyloid β-protein fibrillization. *Proc. Natl. Acad. Sci. U.S.A.* **95**, 12277–12282 (1998).
42. D. Fologea, M. Gershow, B. Ledden, D. S. McNabb, J. A. Golovchenko, J. Li, Detecting single-stranded DNA with a solid state nanopore. *Nano Lett.* **5**, 1905–1909 (2005).
43. E. C. Yusko, R. An, M. Mayer, Electroosmotic flow can generate ion current rectification in nano- and micropores. *ACS Nano* **4**, 477–487 (2010).
44. B. R. Putra, L. Tshwenya, M. A. Buckingham, J. Chen, K. J. Aoki, K. Mathwig, O. A. Arotiba, A. K. Thompson, Z. Li, F. Marken, Microscale ionic diodes: An overview. *Electroanalysis* **33**, 1398–1418 (2021).
45. S. van Dorp, U. F. Keyser, N. H. Dekker, C. Dekker, S. G. Lemay, Origin of the electrophoretic force on DNA in solid-state nanopores. *Nat. Phys.* **5**, 347–351 (2009).

Acknowledgments

Funding: This work was supported by the Japan Society for the Promotion of Science (JSPS) KAKENHI grant number 18H01846 and Scientific Research on Innovative Areas 17H06354.

Author contributions: M.T., Y.B., and T.K. planned and designed experiments. M.T. and A.A. participated in nanothermometer-embedded nanopore fabrications and ionic current/thermovoltage measurements. M.T. and K.Y. analyzed data and performed finite element simulations. M.T., Y.B., and T.K. co-wrote the paper. **Competing interests:** The authors declare that they have no competing interests. **Data and materials availability:** All data needed to evaluate the conclusions in the paper are present in the paper and/or the Supplementary Materials.

Submitted 30 July 2021
Accepted 20 December 2021
Published 11 February 2022
10.1126/sciadv.abl7002